Skeletal Radiol (2015) 44:849–856
DOI 10.1007/s00256-014-2057-5

TECHNICAL REPORT

Metal-induced artifacts in computed tomography and magnetic resonance imaging: comparison of a biodegradable magnesium alloy versus titanium and stainless steel controls

Lukas Filli · Roger Luechinger · Thomas Frauenfelder · Stefan Beck · Roman Guggenberger · Nadja Farshad-Amacker · Gustav Andreisek

Received: 11 August 2014 / Revised: 2 November 2014 / Accepted: 5 November 2014 / Published online: 23 November 2014

Abstract
Objective To evaluate metal artifacts induced by biodegradable magnesium—a new class of degradable biomaterial that is beginning to enter the orthopedic routine—on CT and MRI compared to standard titanium and steel controls.
Methods Different pins made of titanium, stainless steel, and biodegradable magnesium alloys were scanned using a second-generation dual-energy multidetector CT and a 1.5-T MR scanner. In CT, quantitative assessment of artifacts was performed by two independent readers by measuring the noise in standardized regions of interest close to the pins. In MRI, the artifact diameter was measured. Interobserver agreement was evaluated using intraclass correlation coefficients. Artifacts were compared using Mann Whitney U tests.
Results In comparison to stainless steel, biodegradable magnesium alloys induced significantly fewer artifacts in both 1.5-T MRI (p=0.019–0.021) and CT (p=0.003–0.006). Compared to titanium, magnesium induced significantly less artifact-related noise in CT (p=0.003–0.008). Although artifacts were less on MRI for biodegradable magnesium compared to titanium, this result was not statistically significant.
Conclusion Biodegradable magnesium alloys induce substantially fewer artifacts in CT compared to standard titanium and stainless steel, and fewer artifacts in MRI for the comparison with stainless steel.

Keywords Biodegradable implants · Magnesium · Artifacts · Magnetic resonance imaging · Multidetector computed tomography

Abbreviations

CT	Computed tomography
FFE	Fast-field echo
HU	Hounsfield units
kV	Kilovolts
ICC	Intraclass correlation coefficient
mAs	Milliampere-seconds
MRI	Magnetic resonance imaging
ROI	Region of interest
SE	Spin-echo
SEMAC	Slice encoding for metal artifact correction
VAT	View angle tilting

L. Filli · T. Frauenfelder · R. Guggenberger · N. Farshad-Amacker · G. Andreisek
Department of Diagnostic and Interventional Radiology, University Hospital Zurich, Ramistrasse 100, 8091 Zurich, Switzerland

T. Frauenfelder
e-mail: thomas.frauenfelder@usz.ch

R. Guggenberger
e-mail: roman.guggenberger@usz.ch

N. Farshad-Amacker
e-mail: nadja.farshad@usz.ch

G. Andreisek
e-mail: gustav@andreisek.de

R. Luechinger
Institute for Biomedical Engineering, University and ETH Zurich, Ramistrasse 100, 8091 Zurich, Switzerland
e-mail: luechinger@biomed.ee.ethz.ch

S. Beck
Synthes GmbH, 4528 Zuchwil, Switzerland
e-mail: Beck.Stefan@synthes.com

L. Filli (✉)
Department of Radiology, University Hospital Zurich, Ramistrasse 100, CH - 8091 Zurich, Switzerland
e-mail: lukas.filli@usz.ch

Introduction

Metal artifacts arising from commonly used metallic biomaterials, such as stainless steel and titanium, may substantially impair diagnostic image evaluation. In computed tomography (CT), the high attenuation coefficient of metallic implants leads to beam hardening and incomplete attenuation profiles, resulting in streak artifacts [1]. In magnetic resonance imaging (MRI), metallic implants induce changes in the local magnetic field, leading to signal voids and geometric distortion [2]. Despite recent technical developments [3–9], they remain a major issue in daily clinical routine for CT and MRI.

Historically, orthopedic implants consisted almost exclusively of inert alloys, such as stainless steel and titanium. In the past few years, however, potential alternative materials including biodegradable magnesium alloys have gained much interest as they provide several advantages [10, 11]. Most importantly, their biodegradability obviates the need for a secondary surgical removal. In addition, magnesium alloys are lighter than steel and titanium, show excellent interfacial strength, and may actually stimulate new bone growth [10, 11]. These new materials are now entering orthopedic routine [12, 13].

The aim of this study was to evaluate metal artifacts induced by biodegradable magnesium alloys using CT and MRI in comparison to standard titanium and stainless steel controls.

Materials and methods

Four orthopedic pins with the same length (13 cm) made of titanium (diameter, 2.0 mm; chemical composition: Ti–6Al–7Nb), stainless steel (diameter, 2.0 mm), and biodegradable magnesium alloys (two pins with 1.6 and 2.4 mm diameters, respectively; chemical composition: Mg–Y–Nd–HRE [14]) were provided by one of the major vendors (Synthes GmbH, Zuchwil, Switzerland; a company of Johnson&Johnson Inc., New Brunswick, NJ).

CT imaging

The four different metallic pins were scanned using a second-generation dual-energy 128-detector CT scanner (Somatom Definition Flash, Siemens Healthcare, Forchheim, Germany). Scans were performed in the following two scenarios: (1) With the pins embedded in agar, the scanner was operated with two different tube voltages (dual energy mode, 80 and 140 kV, respectively). (2) The pins were surrounded by air, and the system was operated with a constant tube voltage of 120 kV (single-energy mode) and four different tube currents (25, 50, 100, and 200 mAs). Scans were obtained with the pins positioned both parallel and orthogonal to the z-axis.

MR imaging

MRI was performed using a standard 1.5-T scanner (Achieva, Philips Healthcare, Best, The Netherlands). The four pins were placed onto a plastic grid and both the pins and the grid placed in a phantom filled with a CuSO4 solution (1 g CuSO4 per 1 l distilled water; 8 l in total). Imaging was performed at a room temperature of 21 °C and, according to the American Society for Testing and Materials (ASTM) F2119 standard [15], using a fast-field echo (FFE) sequence (TR, 100 ms; TE, 15 ms; flip angle, 15°; acquisition time, 3.15 min) and a standard T1-weighted spin-echo (SE) sequence (TR, 500 ms; TE, 20 ms; flip angle, 70°; acquisition time, 4.22 min). The other imaging parameters were identical for both sequences: slice thickness, 3 mm; matrix, 256×256; receiver bandwidth, 125 Hz/pixel. Scans were acquired parallel and orthogonal to the main magnetic field direction.

Image analysis

In CT, quantitative assessment of artifacts was performed placing standardized regions of interest (ROIs) close to the pins. For pins placed parallel to the z-axis, three circular ROIs (mean size 1.6 cm^2; range 1.3–1.8 cm^2) were placed around each pin. For pins oriented orthogonal to the z-axis, two oval-shaped (mean size 6.2 cm^2; range 5.7–7.0 cm^2) and one circular ROI (mean size 1.5 cm^2; range 1.2–1.9 cm^2) were positioned around each pin. A fourth ROI (mean size 1.6 cm^2; range 1.4–2.0 cm^2) was always placed at the edge of the scan field to measure the background noise. The resulting artifact-induced noise was defined as the mean value of the standard deviation of Hounsfield units (HU) inside the three ROIs corrected by the background noise [16, 17]. The artifact-induced noise measurements were performed by two independent readers blinded to the material and diameters of the pins and to the scan parameters.

In MRI, the same readers performed all measurements by assessing the maximum diameter of the artifacts in the different sequences [6].

Statistical analysis

Statistical analysis was performed using SPSS (version 19, IBM Corp., Somers, NY). For the evaluation of the interobserver agreement, intraclass correlation coefficients (ICCs; absolute agreement, two-way mixed) were calculated and interpreted according to Kundel and Polansky [18]. For CT measurements, separate Mann-Whitney U tests for all different imaging parameters (such as 140 kV) were performed to

compare the noise around the pins. Bonferroni correction for multiple comparisons was applied, resulting in a p-value below 0.05/6=0.008 to indicate statistically significant differences. For MRI measurements, single diameters could not be statistically compared; therefore, the measurements by both observers in parallel and orthogonal orientation were combined for each pin. A p-value of <0.05 was considered to indicate statistically significant differences for these tests [19].

Table 1 Artifact-induced noise in CT caused by different metallic pins positioned parallel and orthogonal to the z-axis, measured by two independent readers. Artifact-induced noise was defined as the mean value of the standard deviation of Hounsfield units (HU) inside the three ROIs corrected by the background noise. Values are presented in HU as mean±standard deviation [minimum-maximum]. Mg, magnesium; R1/R2, reader one/two; ICC, intraclass correlation coefficient

CT parameters	Reader	Titanium	Steel	Mg 1.6	Mg 2.4
Pins placed parallel to the z-axis					
80 kV, 37 mAs	R1	16.7±1.1 [15.2–17.9]	99.0±5.7 [92–107.6]	3.1±1.0 [2.2–4.6]	1.9±0.3 [1.5–2.0]
	R2	13.1±1.8 [13.1–18.0]	93.1±7.4 [85.9–104.2]	3.9±0.6 [3.1–4.8]	1.9±0.5 [1.1–2.5]
	ICC	0.89	0.89	0.83	0.86
120 kV, 25 mAs	R1	6.8±1.7 [4.3–9.2]	27.5±3.3 [22.5–31.6]	1.2±0.3 [0.8–1.6]	2.9±0.3 [2.4–3.3]
	R2	6.8±1.2 [5.0–8.1]	25.2±2.4 [22.8–28.9]	1.1±0.3 [0.6–1.5]	2.5±0.3 [2.1–2.7]
	ICC	0.96	0.85	0.98	0.77
120 kV, 50 mAs	R1	4.2±1.6 [1.9–6.4]	10.9±2.9 [7.9–13.1]	1.9±0.3 [1.4–2.3]	1.4±0.6 [0.7–2.3]
	R2	3.9±0.6 [3.0–4.9]	11.1±2.6 [8.8–12.8]	2.0±1.0 [1.2–3.5]	1.4±0.3 [1.0–1.9]
	ICC	0.87	0.97	0.75	0.93
120 kV, 100 mAs	R1	1.8±0.3 [1.3–2.1]	10.0±1.8 [7.2–12.4]	1.9±0.3 [1.4–2.2]	1.0±0.3 [0.9–1.7]
	R2	1.8±0.3 [1.5–2.2]	11.9±2.0 [9.0–14.9]	1.9±0.3 [1.6–2.4]	1.5±0.3 [1.1–2.0]
	ICC	0.87	0.88	0.91	0.94
120 kV, 200 mAs	R1	1.2±0.9 [0.2–2.6]	7.1±2.2 [3.9–10.3]	1.0±0.3 [0.6–1.5]	1.0±0.3 [0.7–1.5]
	R2	3.0±1.0 [2.2–4.5]	9.8±1.5 [7.6–11.8]	1.1±0.2 [0.9–1.5]	1.5±0.3 [1.1–2.0]
	ICC	0.66	0.77	0.95	0.75
140 kV, 18 mAs	R1	5.6±1.0 [4.1–6.6]	19.3±2.2 [17.2–22.6]	1.2±0.7 [0.5–2.2]	3.0±1.2 [1.3–4.4]
	R2	5.8±1.1 [4.1–7.4]	21.2±2.6 [18.3–25.0]	1.2±0.3 [1.0–1.6]	2.1±0.6 [1.2–3.1]
	ICC	0.97	0.92	0.85	0.84
All measurements (mean±SD)		6.1±5.1	28.9±31.4	1.8±1.1	1.9±0.9
Pins placed orthogonal to the z-axis					
80 kV, 37 mAs	R1	62.2±3.4 [58.2–67.3]	125.6±3.4 [121.6–130.8]	23.9±1.9 [21.0–26.5]	41.6±3.3 [36.6–46.2]
	R2	63.7±5.5 [59.0–72.0]	127.3±5.3 [119.4–131.6]	24.9±1.3 [22.9–26.4]	37.1±3.2 [34.4–41.9]
	ICC	0.94	0.86	0.92	0.74
120 kV, 25 mAs	R1	40.0±4.3 [33.6–45.1]	130.5±8.1 [118.3–141.5]	3.2±0.6 [2.5–4.1]	19.4±1.3 [17.4–20.4]
	R2	35.1±4.2 [28.7–41.0]	133.1±12.3 [118.1–151.6]	3.1±0.8 [1.9–3.8]	22.5±0.9 [21.5–23.9]
	ICC	0.85	0.96	0.91	0.37
120 kV, 50 mAs	R1	37.2±3.7 [32.6–42.8]	108.8±19.2 [80.0–128.8]	4.1±1.2 [3.0–5.9]	21.3±1.3 [19.3–22.4]
	R2	34.0±5.2 [26.2–39.6]	107.0±12.4 [88.4–119.3]	4.9±0.6 [4.4–5.9]	24.5±1.4 [22.6–26.5]
	ICC	0.88	0.97	0.84	0.52
120 kV, 100 mAs	R1	36.4±3.9 [33.5–42.2]	155.0±10.1 [144.1–170.1]	4.9±0.3 [4.4–5.2]	13.3±1.5 [11.0–14.9]
	R2	32.2±2.2 [30.0–35.5]	160.1±13.6 [139.7–178.9]	4.4±1.3 [2.5–5.4]	11.4±1.4 [10.1–13.5]
	ICC	0.73	0.93	0.68	0.72
120 kV, 200 mAs	R1	26.1±1.1 [24.4–27.3]	154.1±2.9 [150.0–158.5]	6.5±0.7 [5.4–7.3]	14.0±1.3 [12.8–15.9]
	R2	27.8±3.2 [25.1–32.6]	148.4±5.2 [140.5–155.4]	5.3±1.0 [4.2–6.8]	14.0±2.4 [11.4–17.6]
	ICC	0.66	0.76	0.74	0.93
140 kV, 18 mAs	R1	25.5±1.5 [23.7–27.7]	39.6±1.8 [38.1–42.3]	13.1±0.8 [12.1–14.3]	12.9±1.1 [11.3–13.9]
	R2	23.1±1.0 [21.8–24.7]	37.3±2.3 [35.3–40.7]	14.7±1.0 [13.2–16.1]	12.3±1.3 [10.3–14.1]
	ICC	0.67	0.83	0.71	0.94
All measurements (mean±SD)		36.9±13.5	118.9±41.5	9.4±7.8	20.3±9.9

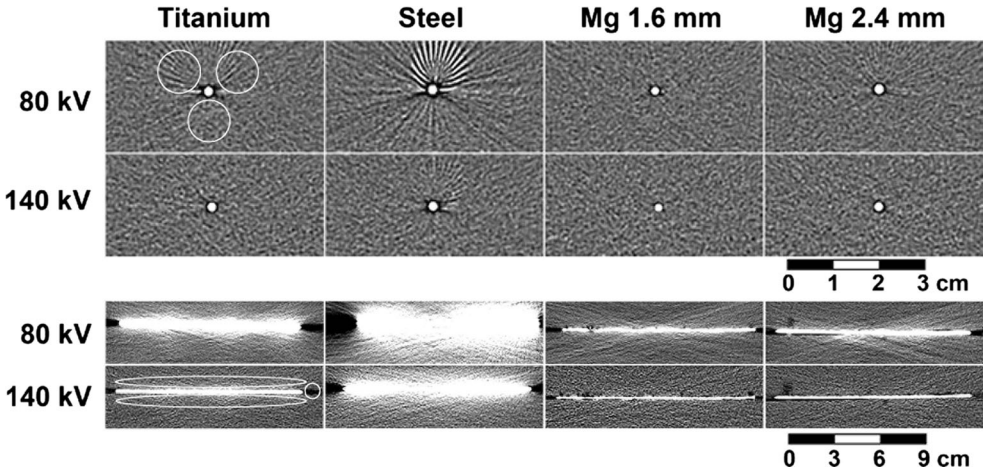

Fig. 1 Two sets of CT images of the four different metallic pins embedded in agar, oriented parallel (*upper set*) and orthogonal (*lower set*) to the z-axis of the CT scanner at a tube voltage of 80 and 140 kV, respectively. Pins from left to right: titanium (diameter, 2.0 mm; chemical composition: Ti–6Al–7Nb), stainless steel (diameter, 2.0 mm), and biodegradable magnesium (1.6 and 2.4 mm diameter, respectively; chemical composition: Mg–Y–Nd–HRE). Window width and level are 400 and 80 HU, respectively. In order to calculate the artifact-induced noise, three circular ROIs were placed around each pin (examples given for the titanium pin). An additional ROI was placed at the edge of the scan field to measure the background noise (not shown)

Results

Artifacts in CT

The interobserver agreement was "substantial" to "almost perfect" (ICC=0.66–0.98) except for the measurements of artifacts induced by the 2.4-mm magnesium pin placed orthogonal to the z-axis at 120 kV/25 mAs (ICC=0.37) and 120 kV/50 mAs (ICC=0.52). Overall mean HU values and standard deviations (SD) of the measured noise around the pins were as follows: titanium (parallel to the z-axis: 6.1±5.1; orthogonal to the z-axis: 36.9±13.5), steel (parallel: 28.9±31.4; orthogonal: 118.9±41.5), magnesium 1.6 mm (parallel: 1.8±1.1; orthogonal: 9.4±7.8), and magnesium 2.4 mm (parallel: 1.9±0.9; orthogonal: 20.3±9.9). Detailed values are provided in Table 1. The artifact-induced noise caused by steel was significantly higher compared with that induced by the titanium and magnesium pins in both parallel and orthogonal measurements, regardless of the imaging parameters used (p=0.003–0.006). Titanium caused significantly higher artifact-induced noise compared with that induced by the different magnesium pins (p=0.003–0.008) except for the measurements with the pins placed parallel to the z-axis at 120 kV/100 mAs and 120 kV/200 mAs (p=0.21–0.86), where both titanium and magnesium similarly induced very little noise (mean values 1.0–3.0 HU) and were thus equivalent (Figs. 1, 2 and 3).

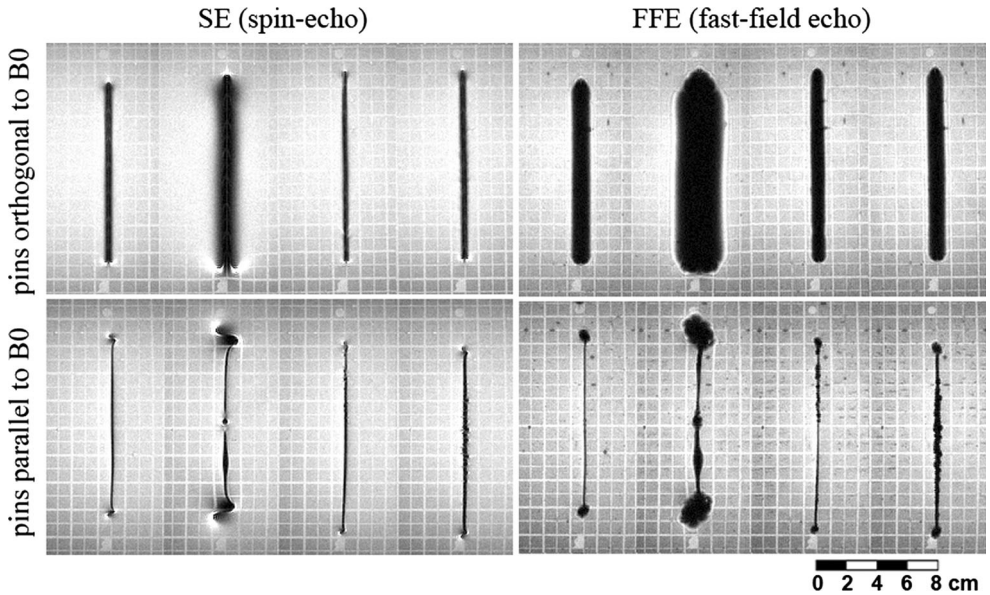

Fig. 2 MRI artifacts induced by the four different metallic pins oriented parallel and orthogonal to the main magnetic field (B0) using spin-echo (SE; TR, 500 ms; TE, 20 ms; flip angle, 70°) and fast-field echo (FFE; TR, 100 ms; TE, 15 ms; flip angle, 15°) sequences. Pins from left to right: titanium (diameter, 2.0 mm; chemical composition: Ti–6Al–7Nb), stainless steel (diameter, 2.0 mm), and biodegradable magnesium alloy (1.6 and 2.4 mm diameter, respectively; chemical composition: Mg–Y–Nd–HRE). The pins were laid on a plastic grid within a phantom filled with CuSO4-doped water

Artifacts in MRI

Overall interobserver agreement was "almost perfect" for the measurements of all pins (ICC: titanium, 0.98; steel, 0.91; magnesium 1.6 mm, 0.95 mm; magnesium 2.4 mm, 0.90). The mean±SD artefact diameters in mm were as follows: titanium (orthogonal to B0: 18.25±1.26; parallel to B0: 11.25±0.96), steel (orthogonal: 41.75±6.13; parallel: 29.5±1.29), magnesium 1.6 mm (orthogonal: 13.0±1.41; parallel: 8.0±0.0), and magnesium 2.4 mm (orthogonal: 15.5±1.73; parallel: 9.25±0.50). Stainless steel induced significantly larger artifacts than all other pins (FFE, SE: p=0.019–0.021) (Table 2, Figs. 2 and 4). No significant differences in MRI artifacts were found between the titanium and different magnesium pins (FFE: p=0.24–0.31; SE: p=0.15–0.48). The artifact diameters measured in the FFE sequence were in total greater than those measured in the SE sequence, but the differences were not statistically significant (p values for the different pins: steel, 0.69; titanium, 0.34; magnesium 2.4 mm, 0.68; magnesium 1.6 mm, 0.49).

Table 2 Maximum artifact diameter [mm] around titanium, stainless steel, and magnesium pins on MR images * measured by two independent readers (R1/R2). Images were acquired using spin-echo (SE; TR, 500 ms; TE, 20 ms; flip angle, 70°) and fast-field echo (FFE; TR, 100 ms; TE, 15 ms; flip angle, 15°) sequences (also see Figs. 2 and 4)

MRI sequence	Titanium 2.0 mm	Steel 2.0 mm	Mg 1.6 mm	Mg 2.4 mm
SE, pins orthogonal to B0	17/18*	37/36	13/11	13/16
FFE, pins orthogonal to B0	20/18	48/46	14/14	16/17
SE, pins parallel to B0	10/12	28/29	8/8	9/9
FFE, pins parallel to B0	11/12	30/31	8/8	10/9

Discussion

Our results showed that biodegradable magnesium induces fewer artifacts than current materials used for orthopedic hardware. This is a promising finding as this new class of degradable biomaterial is beginning to enter orthopedic routine.

It is known that in CT, metal hardware with a low attenuation coefficient generates fewer artifacts [4, 20]. The least artifact arises when the X-ray beam passes the implant at its smallest diameter. In our study, we could also show that the position of the metal hardware is a crucial factor, an effect that was seen for all three materials. However, the positioning of the hardware in relation to the X-ray beam cannot always be influenced in daily clinical routine.

Various correction algorithms for metal artifact reduction in CT exist, and several products have recently become available for clinical use [7, 21]. However, all algorithms have their

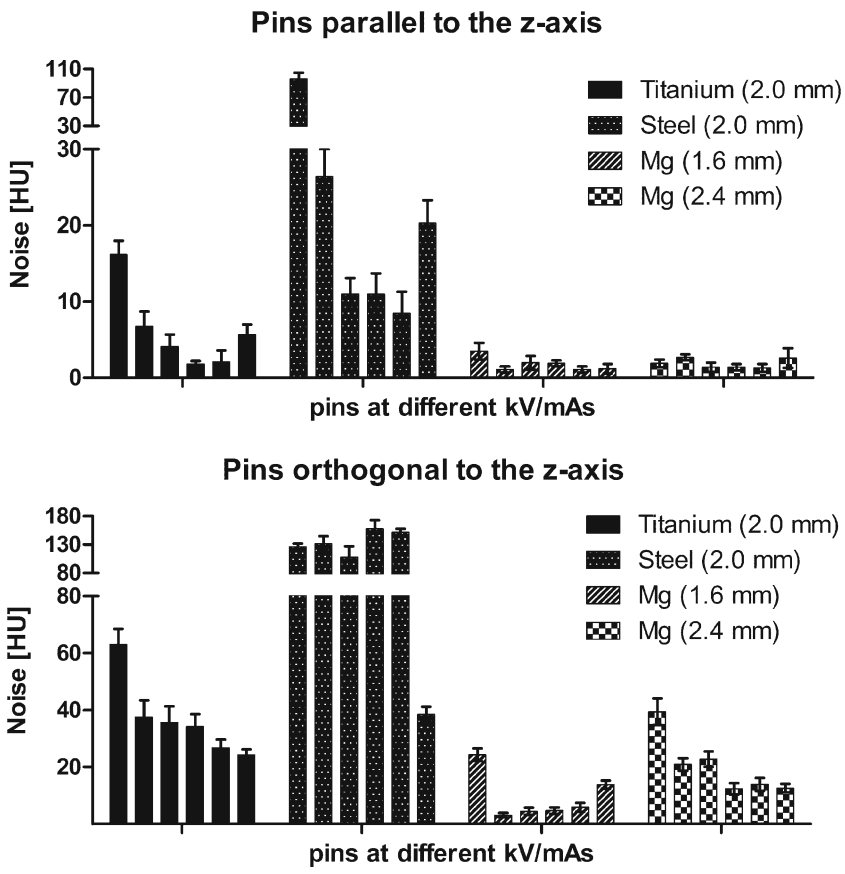

Fig. 3 Artifact-induced noise in CT measured around different metallic pins positioned parallel and orthogonal to the z-axis. All pins were scanned with six different imaging parameters (from left to right): 80 kV/37 mAs, 120 kV/25 mAs, 120 kV/50 mAs, 120 kV/100 mAs, 120 kV/200 mAs, and 140 kV/18 mAs. For clarity reasons, data for both readers (R1, R2) were combined for this figure

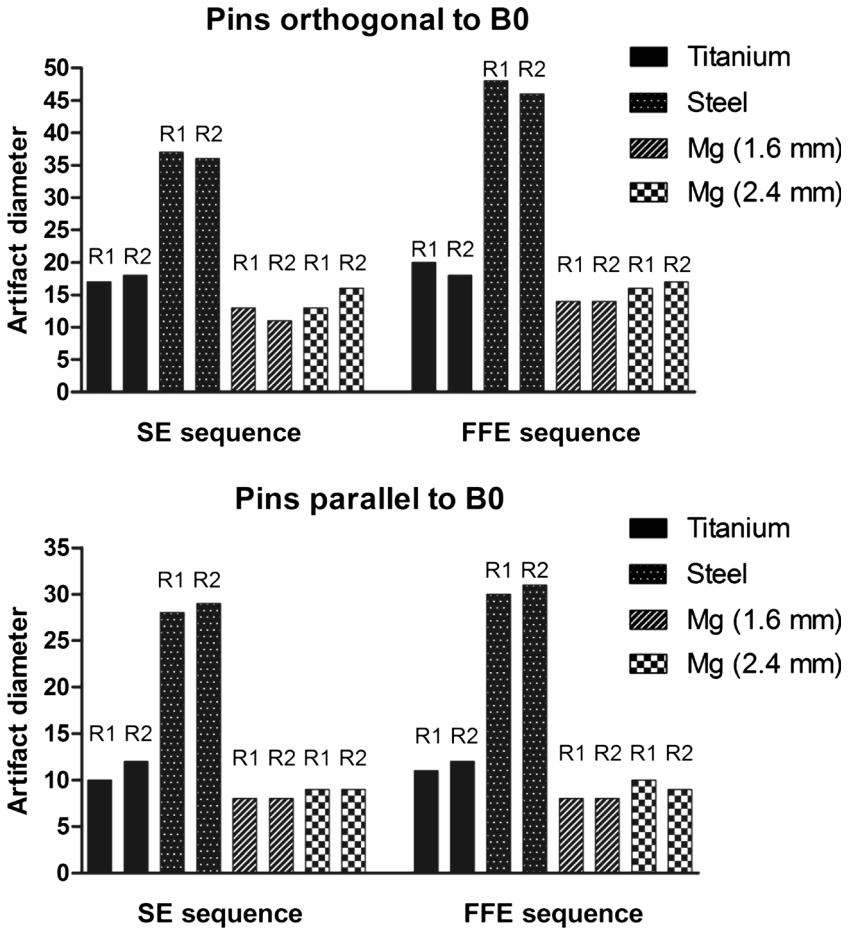

Fig. 4 Maximum artifact diameter around titanium, stainless steel, and magnesium pins on MR images measured by two independent readers (R1, R2). Images were acquired using fast-field echo (FFE; TR, 100 ms; TE, 15 ms; flip angle, 15°) and spin-echo (SE; TR, 500 ms; TE, 20 ms; flip angle, 70°) sequences

inherent limitations, and they may produce other artifacts [3, 5, 17, 22, 23]. To the best of our knowledge, no CT-based study about artifacts induced by biodegradable magnesium alloys has been published so far. Future studies verifying our results are needed, but we do not expect any changes in the principal findings of our study, namely that magnesium alloys are superior to titanium and that both are superior to stainless steel in CT imaging.

Only one previous study has evaluated MRI artifacts caused by biodegradable magnesium alloys. In that study, Ernstberger et al. showed that magnesium-based intervertebral spacers cause a significantly lower total artifact volume in MRI compared with titanium spacers [24]. In our study, we used a more standardized approach with pins placed strictly parallel and orthogonal to the main magnetic field and found that magnesium and titanium hardware produce similar artifacts without a statistically significant difference. According to previous findings [25], smaller artifacts were induced using the SE sequence compared to the FFE sequence; however, these differences were also not statistically significant. Artifacts in MRI can be reduced with optimized imaging parameters, such as increased bandwidth, reduced voxel size, or view-angle tilting [26]. In addition, dedicated metal artifact reduction sequences such as VAT (view angle tilting) or SEMAC (slice encoding for metal artifact correction) have become available recently and are now being evaluated for their performance in clinical studies [8, 9].

A major limitation to successful orthopedic implementation of magnesium alloys was their high corrosion rate and thus premature instability of the hardware [27]. However, new alloys have been developed recently with a significantly lower corrosion rate [28–30], allowing magnesium-based implants to enter orthopedic routine [12]. There are no guidelines yet in the orthopedic literature about when to use them nor about possible indications. Possible indications for postoperative MR include loosening, infection, degradation-related problems, or even small particle disease.

One limitation of this study was the slightly different diameter of the pins, which was due to manufacturing reasons (steel and titanium: 2.0 mm; magnesium: 1.6 and 2.4 mm, respectively). However, even the thick 2.4-mm magnesium pin induced fewer artifacts compared to the smaller 2.0-mm pins made of titanium (in CT) and steel (in both CT and MRI). Second, we only tested pins under standardized conditions in phantoms; clinical situations or near clinical situations (e.g., pins drilled into the bone of cadavers) as well as studies with larger and angulated hardware (e.g., screws, plates, etc.) will likely be more complex and therefore harder to standardize. In

the present study, we tried to standardize all measurements as much as possible (including the use of the ASTM guidelines for the MR experiments), since this was the first technical note study of this new innovative biodegradable material. We agree that further studies are needed to test and discuss the influence of the metal artifact reduction technique for both CT and MR imaging. A third limitation is that there was no iterative reconstruction or any other artifact reduction method used for CT or MR imaging [3, 5, 17, 22, 23]. However, we believe that the use of such methods would not have influenced the results as the inherent artifact effects from the different metal materials would remain. Furthermore, VAT or SEMAC are not yet available for Philips MR systems. Fourth, we did not perform a qualitative analysis, but only a quantitative measurement of the artifacts. Fifth, pins were only evaluated oriented 0° and 90° to the z-axis but not in other angulations (e.g., 45°). Last, in this study, only artifacts were tested. Before successful clinical implementation, the magnesium pins should also be tested for potential heating effects caused by radiofrequency pulses in MRI.

In conclusion, the biodegradable magnesium alloy showed in general fewer artifacts in CT and fewer to similar artifacts in MRI in comparison to standard titanium and stainless steel controls, respectively. This knowledge is important for postoperative imaging, since biodegradable magnesium is entering clinical routine.

Conflict of interest The authors declare no conflict of interest.

References

1. Barrett JF, Keat N. Artifacts in CT: recognition and avoidance. Radiographics Rev Publ Radiol Soc N Am Inc. 2004;24(6):1679–91.
2. Ernstberger T, Heidrich G, Buchhorn G. Postimplantation MRI with cylindric and cubic intervertebral test implants: evaluation of implant shape, material, and volume in MRI artifacting–an in vitro study. Spine J Off J North Am Spine Soc. 2007;7(3):353–9.
3. Prell D, Kyriakou Y, Beister M, Kalender WA. A novel forward projection-based metal artifact reduction method for flat-detector computed tomography. Phys Med Biol. 2009;54(21):6575–91.
4. Lee MJ, Kim S, Lee SA, Song HT, Huh YM, Kim DH, et al. Overcoming artifacts from metallic orthopedic implants at high-field-strength MR imaging and multi-detector CT. Radiographics Rev Publ Radiol Soc N Am Inc. 2007;27(3):791–803.
5. Liu PT, Pavlicek WP, Peter MB, Spangehl MJ, Roberts CC, Paden RG. Metal artifact reduction image reconstruction algorithm for CT of implanted metal orthopedic devices: a work in progress. Skelet Radiol. 2009;38(8):797–802.
6. Harris CA, White LM. Metal artifact reduction in musculoskeletal magnetic resonance imaging. Orthop Clin N Am. 2006;37(3): 349–59. vi.
7. Prell D, Kyriakou Y, Kachelrie M, Kalender WA. Reducing metal artifacts in computed tomography caused by hip endoprostheses using a physics-based approach. Investig Radiol. 2010;45(11): 747–54.
8. Ulbrich EJ, Sutter R, Aguiar RF, Nittka M, Pfirrmann CW. STIR sequence with increased receiver bandwidth of the inversion pulse for reduction of metallic artifacts. AJR Am J Roentgenol. 2012;199(6): W735–42.
9. Koch KM, Brau AC, Chen W, Gold GE, Hargreaves BA, Koff M, et al. Imaging near metal with a MAVRIC-SEMAC hybrid. Magn Reson Med Off J Soc Magn Reson Med/Soc Magn Reson Med. 2011;65(1):71–82.
10. Witte F. The history of biodegradable magnesium implants: a review. Acta Biomater. 2010;6(5):1680–92.
11. Staiger MP, Pietak AM, Huadmai J, Dias G. Magnesium and its alloys as orthopedic biomaterials: a review. Biomaterials. 2006;27(9):1728–34.
12. Windhagen H, Radtke K, Weizbauer A, Diekmann J, Noll Y, Kreimeyer U, et al. Biodegradable magnesium-based screw clinically equivalent to titanium screw in hallux valgus surgery: short term results of the first prospective, randomized, controlled clinical pilot study. Biomed Eng Online. 2013;12:62.
13. Waizy H, Diekmann J, Weizbauer A, Reifenrath J, Bartsch I, Neubert V, et al. In vivo study of a biodegradable orthopedic screw (MgYREZr-alloy) in a rabbit model for up to 12 months. J Biomater Appl. 2013.
14. Castellani C, Lindtner RA, Hausbrandt P, Tschegg E, Stanzl-Tschegg SE, Zanoni G, et al. Bone-implant interface strength and osseointegration: biodegradable magnesium alloy versus standard titanium control. Acta Biomater. 2011;7(1):432–40.
15. ASTM F2119-07. Standard test method for evaluation of MR image artifacts from passive implants: ASTM; 2007.
16. Shinohara Y, Sakamoto M, Iwata N, Kishimoto J, Kuya K, Fujii S, et al. Usefulness of monochromatic imaging with metal artifact reduction software for computed tomography angiography after intracranial aneurysm coil embolization. Acta Radiol. 2013.
17. Guggenberger R, Winklhofer S, Osterhoff G, Wanner GA, Fortunati M, Andreisek G, et al. Metallic artefact reduction with monoenergetic dual-energy CT: systematic ex vivo evaluation of posterior spinal fusion implants from various vendors and different spine levels. Eur Radiol. 2012;22(11):2357–64.
18. Kundel HL, Polansky M. Measurement of observer agreement. Radiology. 2003;228(2):303–8.
19. Tello R, Crewson PE. Hypothesis testing II: means. Radiology. 2003;227(1):1–4.
20. White LM, Buckwalter KA. Technical considerations: CT and MR imaging in the postoperative orthopedic patient. Semin Musculoskelet Radiol. 2002;6(1):5–17.
21. Moon SG, Hong SH, Choi JY, Jun WS, Kang HG, Kim HS, et al. Metal artifact reduction by the alteration of technical factors in multidetector computed tomography: a 3-dimensional quantitative assessment. J Comput Assist Tomogr. 2008;32(4):630–3.
22. Mahnken AH, Raupach R, Wildberger JE, Jung B, Heussen N, Flohr TG, et al. A new algorithm for metal artifact reduction in computed tomography: in vitro and in vivo evaluation after total hip replacement. Investig Radiol. 2003;38(12):769–75.
23. Morsbach F, Bickelhaupt S, Wanner GA, Krauss A, Schmidt B, Alkadhi H. Reduction of metal artifacts from hip prostheses on CT images of the pelvis: value of iterative reconstructions. Radiology. 2013;268(1):237–44.
24. Ernstberger T, Buchhorn G, Heidrich G. Artifacts in spine magnetic resonance imaging due to different intervertebral test spacers: an in vitro evaluation of magnesium versus titanium and carbon-fiber-reinforced polymers as biomaterials. Neuroradiology. 2009;51(8): 525–9.
25. Stradiotti P, Curti A, Castellazzi G, Zerbi A. Metal-related artifacts in instrumented spine. Techniques for reducing artifacts in CT and MRI: state of the art. Eur Spine J Off Publ Eur Spine Soc Eur Spinal Deformity Soc Eur Sect Cervical Spine Res Soc. 2009;18 Suppl 1: 102–8.

26. Sutter R, Ulbrich EJ, Jellus V, Nittka M, Pfirrmann CW. Reduction of metal artifacts in patients with total hip arthroplasty with slice-encoding metal artifact correction and view-angle tilting MR imaging. Radiology. 2012;265(1):204–14.
27. Witte F, Fischer J, Nellesen J, Crostack HA, Kaese V, Pisch A, et al. In vitro and in vivo corrosion measurements of magnesium alloys. Biomaterials. 2006;27(7):1013–8.
28. Wang J, He Y, Maitz MF, Collins B, Xiong K, Guo L, et al. A surface-eroding poly(1,3-trimethylene carbonate) coating for fully biodegradable magnesium-based stent applications: toward better biofunction, biodegradation and biocompatibility. Acta Biomater. 2013;9(10):8678–89.
29. Ostrowski N, Lee B, Enick N, Carlson B, Kunjukunju S, Roy A, et al. Corrosion protection and improved cytocompatibility of biodegradable polymeric layer-by-layer coatings on AZ31 magnesium alloys. Acta Biomater. 2013;9(10):8704–13.
30. Zomorodian A, Garcia MP, Moura EST, Fernandes JC, Fernandes MH, Montemor MF. Corrosion resistance of a composite polymeric coating applied on biodegradable AZ31 magnesium alloy. Acta Biomater. 2013;9(10):8660–70.